# Performance Evaluation of Optically Sensorized Tendons for Articulate Surgical Instruments

**Rohith Karthikeyan**
Department of Mechanical Engineering,
Texas A&M University,
College Station, TX 77840
e-mail: rohithkarthikeyan@tamu.edu

**Kelly Sigmund**
Department of Mechanical Engineering,
Texas A&M University,
College Station, TX 77840

**Yong-Lae Park**
Department of Mechanical Engineering,
Seoul National University,
Seoul 08826, South Korea
e-mail: ylpark@snu.ac.kr

**Seok Chang Ryu**
Department of Mechanical Engineering,
Texas A&M University,
College Station, TX 77840
e-mail: scryu@tamu.edu

*This study proposes an optically sensorized force-sensing tendon for minimally invasive surgical instruments. The tendon is composed of a high strength, polarization maintaining (PM) optical fiber with Bragg sensors (FBGs) that negate the cross-sensitivity of conventional FBGs. The PM-FBG fiber is locally reinforced with high stiffness Kevlar that enhances its load carrying capacity while enabling higher curvatures in tendon routing. The composite tendon has a mean diameter of ∼268 μm which preserves the form-factor of instruments within this scope. Importantly, the tendons can improve the functionality of such tools by enabling local force and tissue-resistance estimation. This paper explores the performance of these sensorized tendons in terms of strength, stability, response under dynamic load, friction, and sensitivity as a force measuring tool within an 18 Ga articulate Nitinol (NiTi) cannula (a proxy for potential applications). Results reaffirm the potential of a bi-modal sensing and actuation component within instruments for robotic surgery.* [DOI: 10.1115/1.4044528]

## 1 Introduction

It has been two decades since the ubiquitous surgical robot, *da Vinci* (Intuitive Surgical, Inc., Sunnyvale, CA), was brought to the medical device market. Due to its clinical and commercial success, surgical robots are poised to revolutionize clinical practice [1]. The next stage along this development path demands a push for robot-assisted minimally invasive surgery (MIS) across therapeutic modalities [2]. This challenge therefore necessitates functionally augmented surgical instruments and miniaturized robotic platforms that are smaller and sophisticated than those currently available [3].

Notably, although robot-assisted procedures using thin, long, and articulate instruments (including the da Vinci system) have profoundly influenced modern surgery, the use of slender tools

inserted through small incisions deprives surgeons of haptic feedback, depth perception, and dexterity [4]. Further, studies suggest that when accurate instrument positioning is required and (or) when the associated structures are fragile such that trauma may have severe implications, the interaction between tool and surrounding tissue can provide useful sensory primitives to the operator [5,6].

The current research on enabling *force-sensing* within such instruments can be broadly classified on the basis of sensor position—proximal (tool-base), distal (near tip/joint), and at the end-effector (gripper) [7]. Each of these alternatives poses unique challenges to instrument design and function. For example, (i) strain gages and push-rod driven load cells [8,9], often seen at the tool-base, are affected by mechanical hysteresis, backlash, and friction; (ii) optical sensors (fiber-bragg gratings or FBGs) and capacitive force-sensors, used at the distal section of the instrument [10,11], are limited by temperature variations and safety considerations, respectively; while (iii) sensors at the end-effector including piezo-resistive elements and strain gages are hindered by size, electromagnetic (EM)-compatibility, and packaging constraints [12].

A potential solution to these challenges would be to integrate multiple robotic functions such as actuation, sensing, and joint motion within a single fundamental element—a *sensorized* tendon. These tendons will serve as both: (i) a force-transmission medium between actuator and joint, and (ii) as an optical strain gage for force-estimation within such instruments (as seen in Fig. 1). The sensor consists of a polarization-maintaining (PM)-FBG sensor that allows for decoupled temperature and strain measurement while using a single FBG sensor (see Appendix A). This fiber is reinforced by a high-stiffness synthetic substrate (Kevlar) that will improve its load carrying capacity and permit complex tethering configurations. The rest of this article discusses our evaluation method for the proposed tendons, in terms of relevant sensor characteristics (sensitivity and friction independence), the effect of fiber reinforcements, and ability to estimate tip-forces when instrumented within a steerable catheter. To the best of the authors' knowledge, this research is the first to introduce such a tendon and demonstrate its performance for microsurgery.
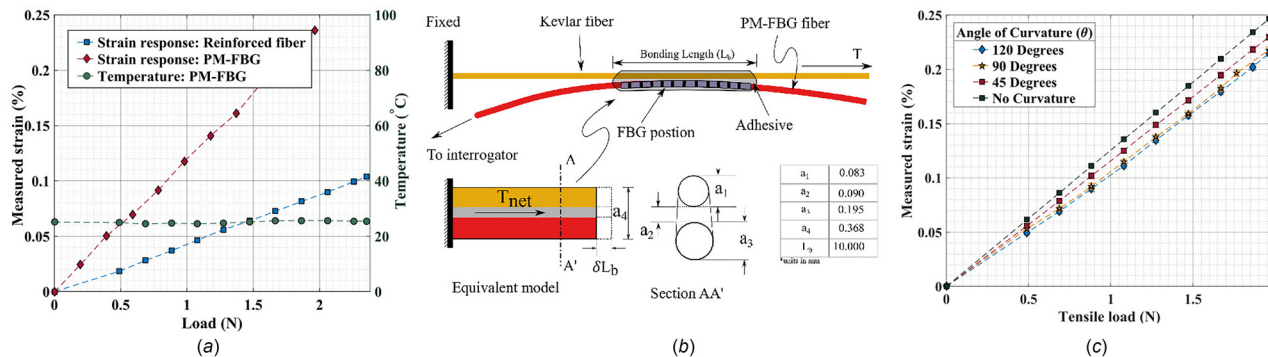
## 2 Performance Evaluation of the Sensorized Tendons

With optical fibers as force-transmission and sensing elements (FBGs) within miniaturized surgical instruments, there are concerns related to sensitivity (to applied load), strength (tensile load capacity), tendon routing (curvature restrictions), and friction decay (contact friction). In the sections to follow, we study these facets of force-sensing in such cable-driven systems and present our observations.
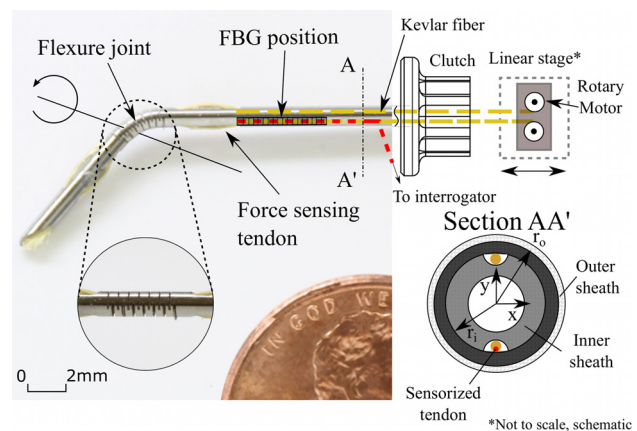


**Fig. 1  A tip-force sensing steerable needle prototype with optical fiber tendons. The 18 Birmingham wire gage needle is 120 mm long, 1.27 mm (0.05″) in diameter and made of superelastic Nitinol. The range of flexion is approximately ±29 deg.**

**Fig. 2 Performance evaluation of sensorized tendons: (*a*) strain and temperature response of the bare PM-FBG fiber and a Kevlar reinforced fiber under tensile loading, (*b*) schematic depicts the PM-FBG fiber reinforced with pretensioned Kevlar fiber, with Kevlar and optical fiber regions separated by an exaggerated adhesive layer, and (*c*) friction decay evidenced from strain response, where, with increasing angle of curvature (corresponding to contact length) and applied load, the recorded strain reduces**

**2.1 Load Sensitivity.** The strain-to-load sensitivity of the PM-FBG fiber provides a measure of its adequacy as a sensing element. To calibrate the PM-FBG fibers and to evaluate their strain response (sensitivity), i.e., percent strain per unit load in tension (%/N), load tests were performed using a bench-top tensile tester machine at room temperature (27 °C). A calibration plot of load against strain and temperature was obtained for the bare fiber (PM-FBG) as shown in Fig. 2(*a*). The load response was linear with a sensitivity of 0.1266%/N. The measured temperature was accurate, stable, and independent of applied strain as evidenced by the figure. This linearity and temperature independence lends confidence to the idea of utilizing PM-FBG fibers as force transmitting tendons, however, concerns to do with permissible load, routing, and curvature remain. We counter these limitations using appropriate reinforcing elements in Sec. 2.2.

**2.2 Reinforcing the Fiber.** The load capacity of the bare fiber was experimentally investigated and contrasted with that of standard telecommunication fibers (see Table 1 in Appendix D). This strength can be further augmented by reinforcing the glass core. Here, we bond the PM-FBG fiber to a strand of pretensioned synthetic para-aramid fiber (Kevlar, DuPont, Wilmington, DE) using an instant alkoxy-ethyl adhesive (Loctite 403, Henkel Adhesives, Dussledorf, Germany) as shown in Fig. 2(*b*). The bonding length was 10 mm and the cure time 24 h. The bonded section can be modeled as a simple composite bar under axial tension. Here, $T_{net}$ is the applied tension that results in an extension, $\delta L_b$, across each layer such that

$$\frac{T_{of}L_b}{A_{of}E_{of}} = \frac{T_{ad}L_b}{A_{ad}E_{ad}} = \frac{T_{kev}L_b}{A_{kev}E_{kev}} \tag{1}$$

where $T$, $A$, $E$, and $L_b$ correspond to applied load across the section, length of the bonded segment, area of cross section, and elastic modulus, respectively. The subscripts of, ad, and kev correspond to optical fiber, adhesive, and Kevlar, respectively. The elastic modulus for Kevlar ($E_{kev}$) = 110 GPa, the optical fiber ($E_{of}$) = 16.56 GPa, and the adhesive ($E_{ad}$) = 3.67 GPa [13,14]. Therefore

$$T_{net} = 2.8123 T_{of} \approx 3(T_{of}) \tag{2}$$

Hence, the effective load transferred to the PM-fiber is approximately one-third the applied load. The plot in Fig. 2(*a*) also depicts the relationship between strain and applied load for the reinforced fiber. This fiber sensitivity is ~0.03975%/N (35% lesser than the bare fiber, as expected from Eq. (1)). Although this entails a drop in sensitivity, the wavelength change to applied-strain threshold of the FBG-interrogator system ($\simeq$1.18 pm/$\mu\epsilon$) enables high-resolution force estimation. Moreover, due to limitations on the bend radius of the glass core in an optical fiber,

reinforcing elements such as Kevlar enable unique tethering configurations that are advantageous to the specific application.

**2.3 Friction Force Independence.** Friction-based force decay is an issue with the use of tendons as transmission elements. Prior research on this topic [15] provides a theoretical model that relates tendon decay to the angle of curvature ($\theta$) and coefficient of friction ($\mu$) between the contact surfaces (reinforced fiber and the polytetrafluoroethane lumen). Although here $\mu$ is small-valued, Fig. 2(*c*) shows an appreciable change in recorded strain with increasing angles of curvature. Within compliant MIS tools, e.g., steerable needles with a tip joint, this hampers the exact decomposition of tip-force, tissue-resistance, and safe tool interactions. An effective solution to mitigate this issue could be to position the sensing element closer to the joint (i.e., reduce contact length). In Fig. 3, we present results from a setup as depicted (inset). A six-axis force-torque sensor (Nano17, ATI Industrial Automation, NC) was mounted on one end of a curved path (contact zone), while the gratings were positioned close to the applied load. The plots show a clear and consistent difference between the calibrated gratings and the F/T sensor due to contact friction; this is in agreement with theory for a fixed angle of curvature (90 deg). Moreover, the load value as recorded by the tendon is close
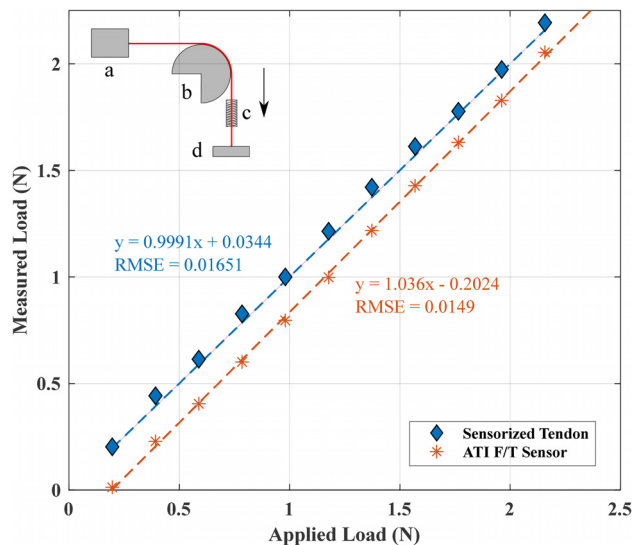


**Fig. 3 Load response comparison between the sensorized tendon and the ATI Nano17 *F/T* sensor along with corresponding fit-data. Schematic (inset): (*a*) ATI Nano17 *F/T* sensor, (*b*) three-dimensional printed structure, (*c*) grating position, and (*d*) applied load.**

to the applied load (RMSE = 0.01651 N). Therefore, placing the sensing element closer to the joint can diminish friction decay.

## 3 Force-Sensing Within Needle-Sized Instruments

The proposed sensorized tendons can be used for microsurgery within steerable instruments, where they can estimate stiffness and reaction forces during tool-tissue interaction. The tool's interaction mechanics and kinematics play an important role in estimating its curvature and deflection. In the sections to follow, we discuss the relevant prerequisites and the methods adopted toward this goal.

**3.1 Tip-Steerable Needle Design.** A prototype instrument was fabricated using a NiTi tube (Confluent Medical, Fremont, CA) having an outer diameter of $1.27 \text{mm}(0.05'', 18 \text{ Ga})$ and a wall thickness of $0.254 \text{ mm}(0.01'')$. A flexure joint was laser-machined onto the tube in the form of circumferential slits. The pattern so machined enables bidirectional, symmetric, and planar bending, and is labeled the bidirectional *flexure*. A single joint segment consists of two circumferential slits arranged opposite to one another. Seven such recurring segments enable up to $\pm 29 \text{ deg}$ of flexion. Two actuation stages of the prototype are shown in Fig. 4(*a*) along with additional design specifications; the net length of the prototype instrument was 120 mm. A plastic (polyether ether ketone) tube was used for the proximal segment to enable follow-the-leader type motion during the insertion experiments (see Sec. 3.6). For the joint, the cutting depth is 0.55 mm ($d_3$), the slit separation is 0.49 mm ($d_4$), and the slit width is 0.06 mm ($d_2$) (see Fig. 4(*a*)). The antagonistic tendons are actuated by a custom manipulator (seen in Fig. 4(*c*)).

**3.2 Tissue Interaction and Stiffness Estimation.** We idealize the behavior of the compliant section (flexure joint) along with the tool-tip to be similar to a cantilever beam as shown in Fig. 4(*b*). Here, the tubular sections which precede and succeed the machined region are assumed to be rigid. The tendon force is $F_{\text{ten}}$ and the inner radius of the tube is $r_i$. The tendon force can be decomposed to account for the pretensioning ($F_{\text{pre}}$) and applied load during extension. This tension force is opposed by (1) device stiffness ($F_{\text{device}}$) and (2) tissue stiffness ($F_{\text{tissue}}$). Therefore, a simple force balance exists and is given by the expression

$$F_{\text{ten}} = F_{\text{pre}} + F_{\text{device}} \pm F_{\text{tissue}} \qquad (3)$$

here, $F_{\text{pre}}$ is a known constant, and we can characterize the effect of device stiffness using the expression below:

$$F_{\text{device}} = \frac{(\text{EI})_{\text{eff}} \times \theta}{L_{\text{flex}} \times r_i} \qquad (4)$$

where $\theta$ is the tip angle obtained from the needle's kinematics, assuming constant curvature bending (see Sec. 3.3), $(\text{EI})_{\text{eff}}$ is the effective rigidity, and $L_{\text{flex}}$ is the length of the flexure joint. Figure 4(*b*) depicts a generalized distributed load at the instrument tip which is attributed to the reaction component from tool-tissue interaction. $F_{\text{tissue}}$ can be estimated by subtracting the known constant $F_{\text{pre}}$ and the calculated $F_{\text{device}}$ from the measured $F_{\text{ten}}$. Further, the tissue reaction ($F_{\text{tissue}}$) can be decomposed into its axial ($F_a$) and transverse components ($F_t$) as indicated in Fig. 4(*b*). We ignore the axial component due to the higher rigidity along the tube axis (i.e., $F_{\text{tissue}} = F_t$). With an appropriate tissue mechanics model, we can extend this to evaluate tissue stiffness ($K_{\text{tissue}}$) using the estimated $F_t$ and tissue displacement ($\delta$) at the tip. To demonstrate the feasibility of this stiffness estimation, in Secs. 3.3–3.5, we employ a simple linear mechanics model, $F_t = K_{\text{tissue}} \times \delta$, where $\delta$ is obtained in correspondence with tip deflection, as a linear function of the tip angle ($\theta$). Figure 5(*b*) presents estimated $F_{\text{tissue}}$ for phantoms over a range of deflection
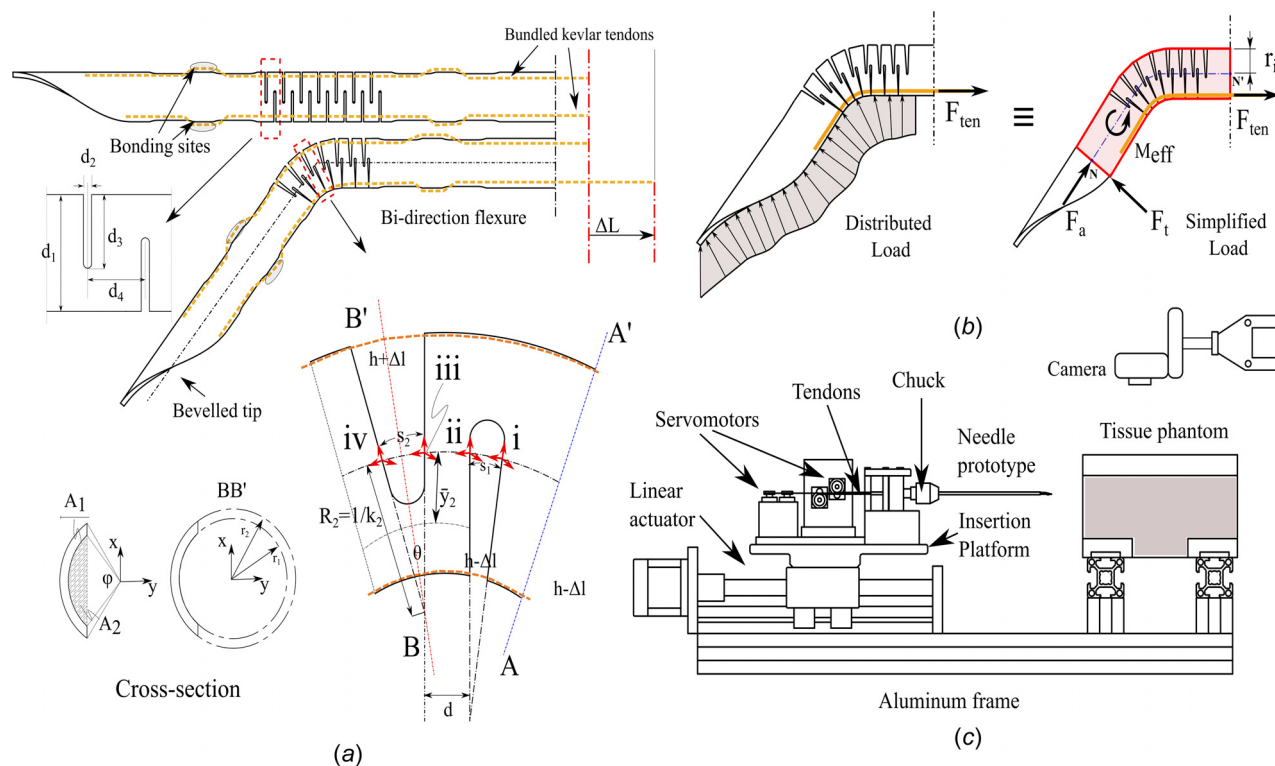
**Fig. 4 Needle kinematic description: (*a*) joint kinematics for the bidirectional planar flexure: section under bending is as shown, with dimensional attributes of a single recurring section and its corresponding geometry under bending load. Reference frames *i* to *iv* and geometric parameters of interest for the recurring section under bending (bottom), (*b*) mechanics model approximation—cantilever beam with an end-moment, and (*c*) schematic of needle steering manipulator used in the experiments.**
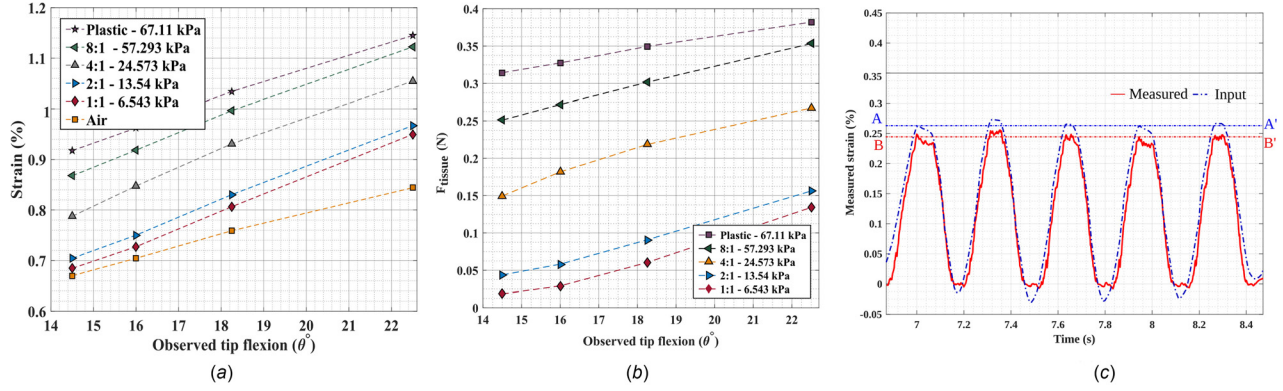
**Fig. 5** (*a*) Static flexion experiment: instrumented prototype actuated within different phantom types; strain response and corresponding tip flexion (ratios correspond to proportion of plastic to thinner in plastisol), (*b*) estimated transverse reaction component $F_{\text{tissue}}$ during static flexion experiments, and (*c*) response of the sensorized tendon under dynamic load at a frequency of 1.38 Hz, an extension of 1.33 m, and net time of 120 s. $AA'$ is the peak-averaged input strain and $BB'$ is the peak-averaged measured strain ($\varepsilon_{\text{of}}$).

values. Appendix B presents a brief summary on tissue property estimation.

### 3.3 Needle Kinematics.

This section describes the kinematic model for the recurring joint segment, building on methods introduced in Ref. [16]. The frame assignments are as depicted in Fig. 4(*a*). Here, the flexure joint is assumed to undergo constant curvature bending. For simplicity, the tendons are assumed to be inextensible and that they remain in complete contact with the walls of the cannula during flexion [17]. The neutral axis of each segment passes through the centroid of their cross section. Hence

$$\overline{y} = \frac{\overline{y_1}A_1 - \overline{y_2}A_2}{A_1 - A_2} \tag{5}$$

where $\overline{y}$ is the distance of the centroid of section $BB'$ from its center. $\overline{y_1}$ and $\overline{y_2}$ are the centroids for sections 1 and 2 as shown in Fig. 4(*a*), while $A_1$ and $A_2$ are their respective areas. The sections $BB'$ and $AA'$ correspond to the slit-section and tube cross sections, respectively. $A_1$ and $A_2$ are given by Eq. (7), with corresponding centroids given by Eq. (6)

$$\overline{y_n} = \frac{4r_n \sin^3(1/2\phi_n)}{3(\phi_n - \sin(\phi_n))} \tag{6}$$

$$A_n = \frac{r_n^2(\phi_n - \sin(\phi_n))}{2} \tag{7}$$

$$\phi_n = 2\cos^{-1}((d_3 - r_2)/r_n) \tag{8}$$

The subscript $n$ corresponds to sections 1 and 2. Based on the deformation geometry of the circumferential slits shown in Fig. 4(*b*), we can map tendon extension ($\Delta l$) to curvature ($k$) using geometric and trigonometric identities

$$\Delta L = h - 2(1/k - r_n)\sin\left(\frac{kh}{2(1 + \overline{y}k)}\right) \tag{9}$$

where $h$ is the initial tendon length under the neutral state of the instrument. This provides the following equations for curvature $k$ and arc length $s$ (the length of the actuating fiber within a deformed slit segment):

$$k_i = \frac{\Delta L}{h(r_n + \overline{y}) - \Delta L\overline{y}} \quad s_i = \frac{h}{1 + \overline{y}k_i} \tag{10}$$

These expressions lead to a sequence of homogeneous transformations from frame $i$ to frame $iv$ (see Fig. 4(*b*)). Together, these

transformations help define the kinematic behavior of the bidirectional flexure joint (also see Appendix C).

### 3.4 Response to Static Loads in Tissue Phantom.

To evaluate the functionality of the sensor instrumented prototype as a force-sensing tool, we performed static flexion experiments within different phantom media. A calibrated sensorized *tendon* was tethered to a needle prototype, held in place by the needle clutch. A camera was used to record tip deflection with tendon extension. The observations indicate that the measured strain is a function of phantom stiffness. The relationship appears linear and remained consistent across trials, which lends credence to the argument that strain data may be reliably calibrated to provide a measure for tissue stiffness under quasi-static operations. Moreover, the difference between the observed strain when in air and within phantom provides an estimate of reaction force from tissue during the static experiments (see Sec. 3.2).

Figure 5(*a*) provides a graphical summary of observed strain as a function of tip flexion and its correspondence to phantom stiffness. The measured strain increases with the increase in tip-flexion and (or) phantom stiffness. Intuitively, we notice that the higher the stiffness, the greater the measured strain for an equivalent extension. The graph in Fig. 5(*b*) presents the response of the transverse reaction force component $F_t$ with the increasing tip flexion. Therefore, the instrumented prototype has a measured strain-to-stiffness sensitivity of 0.003%/kPa, i.e., 35.65 pm/kPa (standard FBG sensitivity is ~1.18 pm/$\mu\epsilon$), i.e., the force resolution is ≃0.027 N.

### 3.5 Response to Dynamic Load.

Needle steering and insertion are dynamic processes; therefore, studying the dynamic behavior of sensorized tendons would further extend its potential application. In these experiments, the pretensioned sensorized tendon was subject to oscillatory loading at different frequencies, extensions (amplitude), and time. Here, the frequency is contingent on actuator RPM (motor speed), extension is dependent on the angular position of the actuator, while the duration of load relies on number of cycles. Under these conditions, applied tendon displacement ($\Delta L_{\text{app}}$) produces two effects—deformation $\Delta L_{\text{def}}$ (strain) and displacement $\Delta L_{\text{disp}}$, which leads to strain across the three media (see Fig. 6).
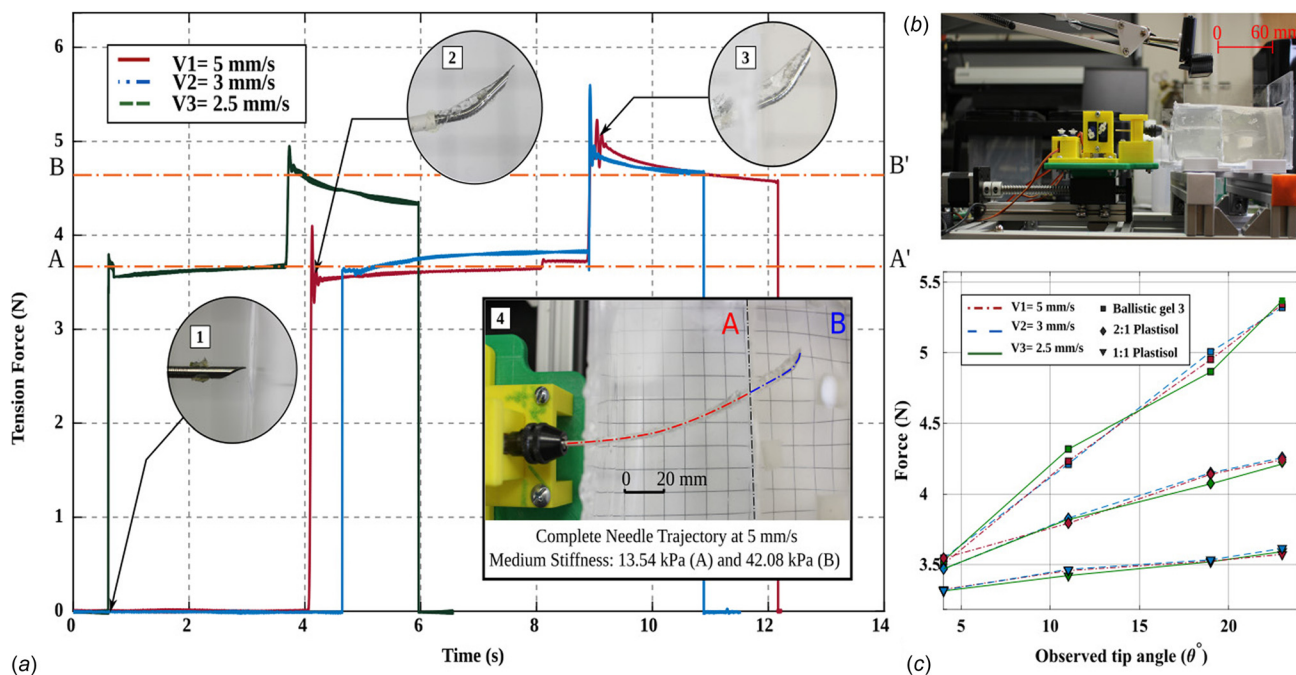
Figure 5(*c*) shows a section of the strain response from a dynamic loading test on the sensorized tendon. Evidently, the observed strain as measured by the gratings is close to applied strain as measured using the optical encoder on the DC motor. The amplitude ratio is ≈0.95 (averaged) and the difference can be attributed to deformation across the adhesive layer. Therefore, under reasonable loading frequencies, amplitude, and duration (as
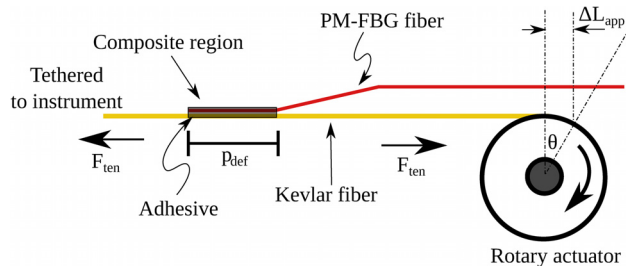
**Fig. 6 Composite model of optical fiber within an adhesive substrate for input strain correspondence in reinforced PM-FBG fiber**

in MIS), the sensor behavior is free of fatigue related hysteresis and associated phenomena (see Table 2), however, there is a discernible change in sensitivity with extended oscillation times, which can be attributed both to adhesive wear and fatigue on the fiber core.

**3.6 Preliminary Insertion Experiments.** The functionality of the instrument during insertion within phantom tissue was experimentally investigated. The sensor-instrumented prototype was tested within three phantoms (ballistic gelatin—42.084 kPa, 2:1 plastisol—13.54 kPa, and 1:1 plastisol—6.543 kPa). Figure 7(c) presents recorded strain and the corresponding force-response from phantom-tool interactions as a function of observed tip-angle. The input variables were insertion velocity (range: 2.5–5 mm/s), phantom stiffness, and deflection angle. The data present the average of four trials. From the graph, the response agrees with the linear trend observed during earlier experiments (see Fig. 5(b)). For comparable flexion angles, the observed strain (and corresponding tension-force) agrees with the measured strain from static insertion trials and is independent of insertion velocity (quasi-static).

In addition, the instrument was interfaced with two-layered phantom arrangements starting with insertion into the more compliant region followed by flexion and crossover onto a stiffer segment (see Fig. 7(a)). During *Stage*-1 (inset), the needle punctures the first phantom layer, while retaining its pretensioned neutral state. Subsequently, tendon deflection (*Stage*-2) causes a rise in observed strain that corresponds to the expected range within the ballistic gelatin, the observed deflection (by imaging) matches the estimated deflection (from needle kinematics) and is maintained by a tension force balance during insertion. *Stage*-3 marks crossover into the stiffer section, and a corresponding rise in the measured strain, independent of insertion velocity and phantom arrangement. The strain behavior agrees with the expected stress-relaxation of visco-elastic tissue phantoms, and the trend is affected by insertion-velocity as evidenced by the varying slopes. Within two-layered phantom arrangements, the observed strain varies with the change in stiffness of the surrounding medium.

## 4 Conclusions

In this paper, we explored a bimodal approach to sensing and actuation in the form of sensorized tendons using Kevlar-reinforced PM-FBG fibers. A potential application in the form of an articulate robotic needle with stiffness/force estimation capabilities was discussed to substantiate this proposition. Although the PM-FBGs are well-understood in their function, to the best of the author's knowledge, this research is the first demonstration of its performance as a bimodal sensing tool in an MIS device.

The results suggest that the tendons are able to transmit loads higher than 40 N, which are substantively more than those previously documented for standard optical fibers (no-gratings). Besides, they provide for temperature-independent strain measurements and a means for friction compensation in tendon-driven robots. The load-to-strain sensitivity of the reinforced fiber is documented to be $0.03975\%/N$ with FBG sensitivity at $1.18$ pm/$\mu\epsilon$ (force resolution $\simeq 0.027\,N$).



**Fig. 7 (a) Plot from insertion into two phantom layers at three different insertion velocities. Images (inset): (1) puncture without tip-flexion, (2) tip-flexion up to 29 deg, (3) crossover into second phantom layer and (4) net trajectory of needle prototype (A—gelatin, B—plastisol), where AA' corresponds to the measured strain average within phantom A and BB' within phantom B. (b) side-view of the insertion test platform, and (c) strain response as a function of flexion angle under varying insertion speeds and phantom compliance.**

When instrumented within the prototype needle, their response to static loads is consistent, linear, and a function of phantom compliance, and flexion angle. This attribute further extends to dynamic loading conditions, where the documented strain is independent of the tested loading frequencies, amplitudes, and (or) time. Together, these factors add to the force-sensing capabilities of the instrument given the complex nature of tool-tissue interactions.

Further, with the addition of a robust tissue-mechanics model, we could extend this toward tissue stiffness estimation, an attribute we explored briefly in this study through a simplified linear approximation, and preliminary insertion experiments. Given the form-factor, cost, and functional demands of surgical instruments today, the tendons show potential for use by reducing tool dimensions and enabling flexibility in sensor-positioning. However, several challenges still remain—standardization of fabrication techniques and calibration methods, susceptibility to torsion, and the need for a robust tissue-mechanics model; these are all concerns to be addressed prior to wider application, and it remains the theme of our current and future work.

## Appendix A: Principle of Polarization Maintaining Fiber With Bragg Sensors Fibers

The ability to decouple strain from temperature has been explored using Bragg gratings written on highly birefringent fiber in conjunction with accurate interrogation techniques. The PM-FBGs have double Bragg reflection peaks (see Fig. 8(a)) with dissimilar sensitivities, which enable the decoupled measurement of strain and temperature. The linear birefringence introduced within the PM fibers preserves the polarization state of the transmitted spectrum. Figure 8(a) depicts consecutive sampling instances at time $t_1$ and $t_2$. Here, a represents peak separation at time instant $t_1$ and b at time $t_1$. The strain ($\epsilon$) and the temperature ($T$) response to wavelengths $\lambda 1$ and $\lambda 2$ are described by the equations that follow (see Fig. 9)

$$
\begin{aligned}
\Delta T &= (A\Delta\lambda_1 - B\Delta\lambda_2)/k \\
\Delta\epsilon &= (C\Delta\lambda_1 - \Delta\lambda_2)/k
\end{aligned} \tag{A1}
$$

where $\Delta\lambda_1$ and $\Delta\lambda_2$ are the change in peak wavelengths with respect to a reference wavelength at known temperature and strain. The sensitivity parameters A, B, C, and D for $\epsilon$ and $T$ are derived empirically, while $k = $ AD–BC (see Refs. [18] and [19] for more information).
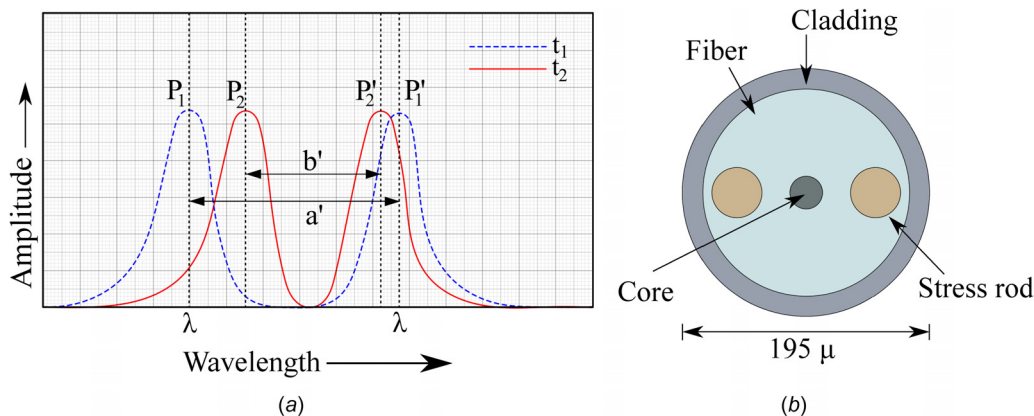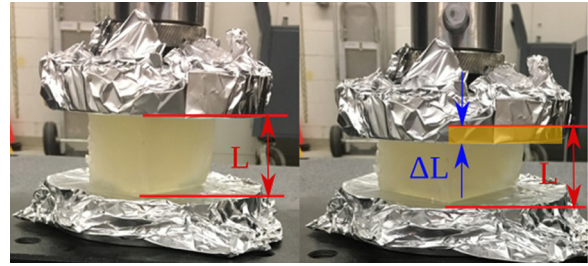


**Fig. 9 Phantom compression tests using Instron 5960 bench-top compression test setup**

## Appendix B: Phantom Fabrication and Properties

The sensor instrumented needle prototype was tested within tissue phantoms of varying stiffness. Two material combinations were used—plastic and thinner (MF Plastics, Fort Worth, TX) and medical grade ballistic gelatin (Clear Ballistics, Inc., Fort Smith, AK). Phantom compliance is varied by changing the proportion of plastic to thinner in solution. A bench-top compression test apparatus (Instron 5960, Instron Corporation, UK) was used to determine their elastic moduli. Phantoms of known dimension were fabricated using standard molds; the specimen were then subject to compressive loads under a consistent strain rate (0.1 in/min) as shown in Fig. 5(a). The applied load and the corresponding strain were recorded. The elastic modulus for each specimen was then determined.

## Appendix C: Needle Kinematics Continued

$$
H_i^{iv} = \begin{bmatrix}
1 & 0 & 0 & 0 \\
0 & \cos^2(k_2 s_2) & B_{22} & B_{33} \\
0 & -B_{22} & -\sin^2(k_2 s_2) & C_{33} \\
0 & 0 & 0 & 1
\end{bmatrix} \tag{A2}
$$

where

$$
\begin{aligned}
B_{33} &= \frac{-\sin(k_2 s_2)(dk_1 + \sin(k_2 s_2))}{k_1} \\
B_{22} &= \cos(k_2 s_2)\sin(k_2 s_2) \\
D_{33} &= \frac{\cos(k_2 s_2)(dk_1 + \sin(k_2 s_2))}{k_1}
\end{aligned}
$$

Therefore, the net transformation for a single segment is



**Fig. 8 (a) Typical spectral response of a single PM-FBG fiber and (b) cross section of the PM-FBG fiber (panda-section)**

$$H_j^{j+1} \equiv \prod_{k=i}^{iv}\{H_k^{k+1} T_z\{d\}\} \qquad \text{(A3)}$$

$$\{H_0^n\}_{\text{net}} = \prod_{j=1}^{n} H_j^{j+1} \qquad \text{(A4)}$$

for $n\,(=7)$ such segments

Equation (A4) provides the mapping between tendon displacement and tip deflection ($\theta$) for the flexure joint.

## Appendix D: Supplementary Tables

**Table 1   Results from tensile loading experiments on standard telecommunication fibers and high strength PM-FBG fibers**

| | Fiber type | Coating diameter $\mu m$ | Cladding diameter $\mu m$ | Core diameter $\mu m$ | Failure load N | Coating material |
|---|---|---|---|---|---|---|
| 1 | Nufern MM-S105/125-22A | $245.0 \pm 15.0$ | $125 \pm 2.0$ | $105 \pm 3.0$ | 9.81 | Acrylate |
| 2 | Nufern 1310M-HP- 80 | $165.0 \pm 10.0$ | $80 \pm 1.0$ | 6.0 | 5.4 | Acrylate |
| 3 | Nufern 1550B-HP | $245.0 \pm 15.0$ | $125 \pm 1.0$ | 9.0 | 11.8 | Acrylate |
| 4 | DTG PM FBG | $195 \pm 15$ | $125 \pm 2.0$ | 6.0 | > 13 (3% strain) | OrMoCer |

**Table 2   A summary of strain response from dynamic tension-slack tests on the instrumented prototype for three scenarios—(a) time: changing oscillation count (up to 200 s), (b) amplitude: increasing extension length (0.89–2.25 mm), and (c) frequency: actuator RPM (up to 5 Hz)**

| Changing parameter | No. of oscillations—time | | | | | Pulling length—extension | | | | Motor speed—frequency | | | |
|---|---|---|---|---|---|---|---|---|---|---|---|---|---|
| Trial No. | T1 | T2 | T3 | T4 | T5 | T1 | T2 | T3 | T4 | T1 | T2 | T3 | T4 |
| Tendon displacement (mm) | | | 1.77 | | | 2.22 | 1.77 | 1.33 | 0.89 | | | 1.77 | |
| Motor speed (RPM) | | | 9.5 | | | | | 9.5 | | 9 | 11 | 13.6 | 16.7 |
| Measured strain $\varepsilon_2$ (%) | 0.298 | 0.292 | 0.299 | 0.309 | 0.297 | 0.359 | 0.298 | 0.239 | 0.178 | 0.308 | 0.303 | 0.307 | 0.306 |
| Amplitude ratio | 0.9426 | 0.9524 | 0.9347 | 0.9834 | 0.9703 | 0.9411 | 0.9767 | 0.9336 | 0.9426 | 0.9677 | 0.9720 | 0.9608 | 0.9366 |
| No. of oscillations | 20 | 30 | 40 | 50 | 60 | | | 20 | | | | 50 | |
| Frequency (Hz) | 2.857 | 2.616 | 2.761 | 2.730 | 2.754 | 2.857 | 1.744 | 1.380 | 1.092 | 2.730 | 3.265 | 4.075 | 5.090 |

The measured strain corresponds to peak averaged values over multiple cycles.

## References

[1] Taylor, R. H., Menciassi, A., Fichtinger, G., and Dario, P., 2008, "Medical Robotics and Computer-Integrated Surgery," *Springer Handbook of Robotics*, Springer, Berlin, pp. 1199–1222.

[2] Daouadi, M., Zureikat, A. H., Zenati, M. S., Choudry, H., Tsung, A., Bartlett, D. L., Hughes, S. J., Lee, K. K., Moser, A. J., and Zeh, H. J., 2013, "Robot-Assisted Minimally Invasive Distal Pancreatectomy Is Superior to the Laparoscopic Technique," Ann. Surg., **257**(1), pp. 128–132.

[3] Corcione, F., Esposito, C., Cuccurullo, D., Settembre, A., Miranda, N., Amato, F., Pirozzi, F., and Caiazzo, P., 2005, "Advantages and Limits of Robot-Assisted Laparoscopic Surgery: Preliminary Experience," Surg. Endoscopy Other Interventional Tech., **19**(1), pp. 117–119.

[4] Tholey, G., Desai, J. P., and Castellanos, A. E., 2005, "Force Feedback Plays a Significant Role in Minimally Invasive Surgery: Results and Analysis," Ann. Surg., **241**(1), pp. 102–109.

[5] Wagner, C., Stylopoulos, N., and Howe, R., 2002, "Force Feedback in Surgery: Analysis of Blunt Dissection," Tenth Symposium on Haptic Interfaces for Virtual Environment and Teleoperator Systems, Orlando, FL, Mar. 24–25, pp. 68–74.

[6] Reiley, C. E., Akinbiyi, T., Burschka, D., Chang, D. C., Okamura, A. M., and Yuh, D. D., 2008, "Effects of Visual Force Feedback on Robot-Assisted Surgical Task Performance," J. Thorac. Cardiovasc. Surg., **135**(1), pp. 196–202.

[7] Lee, D.-H., Kim, U., Gulrez, T., Yoon, W. J., Hannaford, B., and Choi, H. R., 2016, "A Laparoscopic Grasping Tool With Force Sensing Capability," IEEE/ASME Trans. Mechatronics, **21**(1), pp. 130–141.

[8] Trejos, A., Patel, R., Naish, M., Lyle, A., and Schlachta, C., 2009, "A Sensorized Instrument for Skills Assessment and Training in Minimally Invasive Surgery," ASME J. Med. Devices, **3**(4), p. 041002.

[9] He, C., Wang, S., Sang, H., Li, J., and Zhang, L., 2014, "Force Sensing of Multiple-Dof Cable-Driven Instruments for Minimally Invasive Robotic Surgery," Int. J. Med. Rob. Comput. Assisted Surg., **10**(3), pp. 314–324.

[10] Elayaperumal, S., Bae, J. H., Daniel, B. L., and Cutkosky, M. R., 2014, "Detection of Membrane Puncture With Haptic Feedback Using a Tip-Force Sensing Needle," IEEE/RSJ International Conference on Intelligent Robots and Systems (IROS 2014), Chicago, IL, Sept. 4–18, pp. 3975–3981.

[11] Gijbels, A., Vander Poorten, E. B., Stalmans, P., and Reynaerts, D., 2015, "Development and Experimental Validation of a Force Sensing Needle for Robotically Assisted Retinal Vein Cannulations," IEEE International Conference on Robotics and Automation (ICRA), May 26–30, Seattle, WA, pp. 2270–2276.

[12] Kim, U., Lee, D.-H., Yoon, W. J., Hannaford, B., and Choi, H. R., 2015, "Force Sensor Integrated Surgical Forceps for Minimally Invasive Robotic Surgery," IEEE Trans. Rob., **31**(5), pp. 1214–1224.

[13] Pigeon, F., Pelissier, S., Mure-Ravaud, A., Gagnaire, H., and Veillas, C., 1992, "Optical Fibre Young Modulus Measurement Using an Optical Method," Electron. Lett., **28**(11), pp. 1034–1035.

[14] Cease, H., Derwent, P., Diehl, H., Fast, J., and Finley, D., 2006, "Measurement of Mechanical Properties of Three Epoxy Adhesives at Cryogenic Temperatures for CCD Construction," Fermi National Accelerator Laboratory, Batavia, IL.

[15] Palli, G., Borghesan, G., and Melchiorri, C., 2009, "Tendon-Based Transmission Systems for Robotic Devices: Models and Control Algorithms," IEEE International Conference on Robotics and Automation (ICRA'09), Kobe, Japan, May 12–17, pp. 4063–4068.

[16] York, P. A., Swaney, P. J., Gilbert, H. B., and Webster, R. J., 2015, "A Wrist for Needle-Sized Surgical Robots," IEEE International Conference on Robotics and Automation (ICRA), Seattle, WA, May 26–30, pp. 1776–1781.

[17] Camarillo, D. B., Milne, C. F., Carlson, C. R., Zinn, M. R., and Salisbury, J. K., 2008, "Mechanics Modeling of Tendon-Driven Continuum Manipulators," IEEE Trans. Rob., **24**(6), pp. 1262–1273.

[18] Ibrahim, S. K., O'Dowd, J., McCue, R., Honniball, A., and Farnan, M., 2015, "Design Challenges of a High Speed Tunable Laser Interrogator for Future Spacecraft Health Monitoring," CLEO: Applications and Technology, Optical Society of America, San Jose, CA, May 10–15, p. ATu1M–3.

[19] Ibrahim, S. K., Farnan, M., Karabacak, D. M., and Singer, J. M., 2016, "Enabling Technologies for Fiber Optic Sensing," SPIE Photonics Europe, International Society for Optics and Photonics, Brussels, Belgium, Apr. 3–7, p. 98990.